

Learning A Unified 3D Point Cloud for View Synthesis

Meng You, Mantang Guo, Xianqiang Lyu, Hui Liu, and Junhui Hou, *Senior Member, IEEE*

Abstract—3D point cloud representation-based view synthesis methods have demonstrated effectiveness. However, existing methods usually synthesize novel views only from a single source view, and it is non-trivial to generalize them to handle multiple source views for pursuing higher reconstruction quality. In this paper, we propose a new deep learning-based view synthesis paradigm, which learns a unified 3D point cloud from different source views. Specifically, we first construct sub-point clouds by projecting source views to 3D space based on their depth maps. Then, we learn the unified 3D point cloud by adaptively fusing points at a local neighborhood defined on the union of the sub-point clouds. Besides, we also propose a 3D geometry-guided image restoration module to fill the holes and recover high-frequency details of the rendered novel views. Experimental results on three benchmark datasets demonstrate that our method outperforms state-of-the-art view synthesis methods to a large extent both quantitatively and visually. The code will be publicly available at <https://github.com/mengyou2/PCVS>.

Index Terms—Image-based rendering, view synthesis, 3D point clouds, deep learning.

I. INTRODUCTION

Given a collection of posed images observed from source views, view synthesis aims at generating photorealistic images at novel views. As view synthesis can benefit a variety of applications, e.g., robotics [1], 3D modeling [2, 3], virtual reality [4], and so on, a considerable number of view synthesis methods [5, 6, 7, 8, 9, 10] have been proposed over the past decades. Particularly, 3D point cloud representation-based methods, which generally render novel views from 3D scene representations, e.g., 3D point clouds/meshes, have been attracting attention.

Fig. 1 shows paradigms of different 3D point cloud representation-based view synthesis methods. Specifically, some methods [11, 12, 13, 14, 15, 16] illustrated in Fig. 1 (a) require inputting the full 3D point cloud, which maybe difficult and labor-intensive to obtain. Conversely, other methods [17, 18, 19] shown in Fig. 1 (b) construct the point cloud from a single source view by predicting its depth map and further projecting the source view to 3D space. In reality, it is easy to obtain multiple source views of a scene, which may greatly improve the quality of the novel view synthesis. Unfortunately,

it is not straightforward to generalize the single view-based paradigm shown in Fig. 1 (b) to handle multiple input source views well. To synthesize novel views from more than one source view [20], as shown in Fig. 1 (c), one can simply extend the single view-based paradigm, i.e., separately generating an intermediate novel view from each source view, and then fusing the intermediate results via a confidence-based blending module. However, such a manner cannot take advantage of the relationship between different source views well, thus limiting its performance (see Section IV for the results).

To this end, we propose a new deep learning-based paradigm for view synthesis, as illustrated in Fig. 1 (d), which learns a unified 3D point cloud by adaptively fusing the sub-point clouds constructed from different source views. Specifically, we first project pixels of each source view into 3D space with corresponding depth maps, leading to sub-point clouds. As the depth maps are not perfect and inevitably contain errors, we adaptively fuse the sub-point clouds to a unified 3D point cloud representation with better quality via a point cloud fusion module. Besides, we propose a 3D geometry-guided image restoration module to fill holes and recover high-frequency details in the rendered novel view. Extensive experiments on three benchmark datasets demonstrate the significant superiority of our method over state-of-the-art view synthesis methods both quantitatively and visually. Besides, comprehensive ablation studies validate the effectiveness of the key modules of our framework.

In summary, the main contributions of this paper are three-fold:

- a new learning-based paradigm of point cloud representation-based view synthesis from multiple source views;
- a learnable point cloud fusion module to construct a unified point cloud representation of the input scene; and
- a 3D geometry-guided image restoration module to fill holes and recover high-frequency details of the rendered novel view.

The rest of this paper is organized as follows. Section II briefly reviews related works. Section III presents the proposed framework for view synthesis, followed by comprehensive experiments and analyses in Section IV. Finally, Section IV concludes the paper.

II. RELATED WORK

View synthesis is a long-standing problem in computer vision/graphics. Traditional methods [21, 22, 23, 24, 25] implement image-based rendering with the idea of blending

This work was supported in part by the Hong Kong Research Grants Council under Grants 11218121 and 21211518, and in part by the Basic Research General Program of Shenzhen Municipality under Grant JCYJ20190808183003968. *Corresponding Author: Junhui Hou.*

M. You, M. Guo, X. Lyu, and J. Hou are with the Department of Computer Science, City University of Hong Kong, Hong Kong, and also with the City University of Hong Kong Shenzhen Research Institute, Shenzhen 518057, China. (e-mail: jh.hou@cityu.edu.hk)

H. Liu is with the School of Computing Information Sciences, Caritas Institute of Higher Education, Hong Kong. (e-mail: hliu99-c@my.cityu.edu.hk)

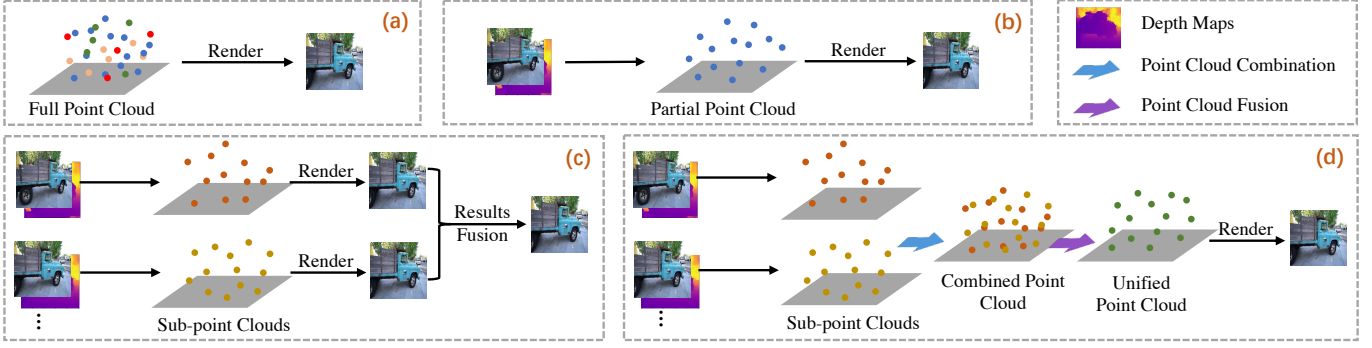


Fig. 1. Comparison of different point cloud representation-based view synthesis paradigms.

synthesized images from source views. However, they are usually time-consuming and require dense inputs to achieve high-quality results. Recently, the powerful deep learning has been widely used in the view synthesis area. Some methods [5, 6, 7, 8] perform pixel interpolation in the novel view by employing a neural network to estimate appearance flow between viewpoints. These methods lack scene geometry in their models, thus limiting their performance, especially for real scenes. To overcome these limitations, some methods attempt to explicitly utilize the scene geometry by learning scene representations from large datasets. These methods first reconstruct 3D geometry, such as volumetric representations, point cloud representations, and neural representations, from images, and then render novel views.

A. Volumetric Representation-based Methods

Recently, some methods learn the volumetric representations, such as voxel-based grid, multi-plane image (MPI), or layered depth image (LDI), from source images. Specifically, the voxel-based grid methods [26, 27, 28, 29, 30, 31, 32, 33] represent objects as a 3D volume in the form of voxel occupancies. Kar *et al.* [29] utilized the underlying 3D geometry in multi-view images to reconstruct the voxel occupancy grid by unprojecting image features along with viewing rays. Sitzmann *et al.* [34] proposed DeepVoxels to encode the view-dependent appearance of the scene without explicitly modeling its 3D geometry. MPI [35, 36, 37, 38, 39] represents the scene as a set of fronto-parallel planes at fixed depths, where each plane consists of an RGB image and an α map. Mildenhall *et al.* [37] proposed to expand each input view into an MPI, and then render the novel view by blending its adjacent MPIs. Li *et al.* [39] built the DeepMPI representation by adding latent features in MPI layers to render view-dependent lighting effects. Similar to MPI, LDI [40, 41, 42, 43, 44] keeps several depth and color values at every pixel, and renders images by a back-to-front forward warping algorithm. Tulsiani *et al.* [42] used convolutional neural networks (CNN) to infer LDI representation from a single image and forward splitting pixels to render a novel view. Shih *et al.* [43] proposed to generate LDI from RGBD images, and employ a learning-based inpainting model to synthesize the color and depth information at occluded regions. Choi *et al.* [45] and Shi *et al.* [10] constructed the depth probability volume of the

novel view to backward warp color images or feature maps from source views. Because of their discrete sampling, these mentioned volumetric representation-based methods cannot achieve high-resolution results.

B. 3D Point Cloud Representation-based Methods

Given the point cloud associated with descriptors, some methods [11, 12, 13, 16] rasterize the point cloud into 2D image space with a learning-based differentiable rendering scheme. Instead of explicitly rendering the point cloud representation, Dai *et al.* [14] and Song *et al.* [15] proposed to extract features from the point cloud representation to construct a multi-plane 3D representation, and then render the color image from it via a neural network. Other methods [46, 47] use the point cloud as a base geometry model, which is further fitted to a surface mesh, and generate novel views by blending weights of sources on the mesh surface. Some methods construct the point cloud by estimating the depth maps of source views. Niklaus *et al.* [17] proposed to predict the depth map of the source view guided by semantic information, and then render the novel view from the colored point cloud constructed from the source view based on the estimated depth map. Wiles *et al.* [18] projected the feature map of the source view to the 3D space based on the estimated depth map, and then synthesized novel view by decoding the feature map rendered from the point cloud. Le *et al.* [19] proposed to backward warp the synthesized novel view to the source one to supervise the depth estimation of the source view. Cao *et al.* [20] forward warped each input view with a differentiable point cloud renderer similar to [18], but extended to multiple inputs by fusing rendered view-dependent features.

C. Neural Scene Representation-based Methods

More recent methods represent the scene as neural radiance field (NeRF) by learning a continuous volumetric scene function [9]. Martin *et al.* [48] extended NeRF to handle a collection of in-the-wild images. To tackle the problem that NeRF requires to be re-trained before generalizing to other unobserved scenes, some methods [49, 50, 51, 52, 53, 54] focus on NeRF generalization by involving the scene prior at the training phase. Yu *et al.* [49] attached image features behind the inputs of the NeRF. Wang *et al.* [50] combined

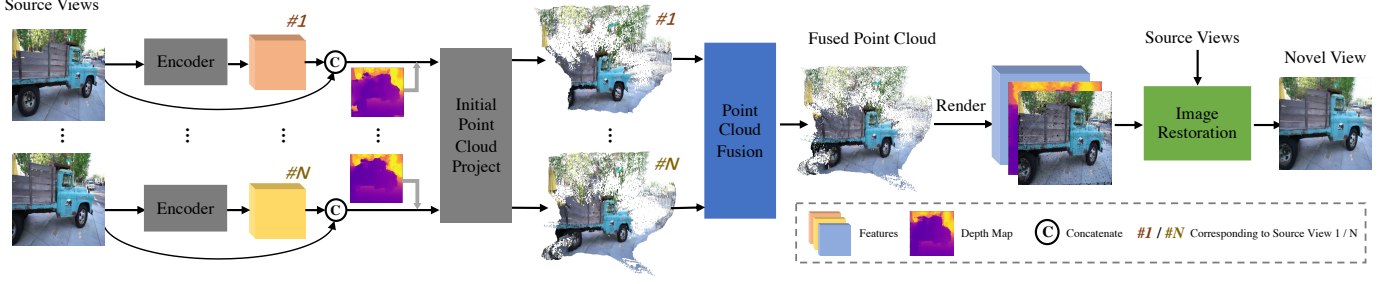


Fig. 2. Flowchart of the proposed framework for view synthesis from multiple source views. It is mainly composed of two parts, i.e., learning of the unified point cloud from multiple sub-point clouds of input views and 3D geometry-guided image restoration, which are detailed in Fig. 3 and Fig. 4, respectively.

image-based rendering method with NeRF by aggregating input image features to estimate visibility and blend colors simultaneously. Chibane *et al.* [52] introduced the classical multi-view stereo ideas into NeRF, predicting RGB and density for each 3D point from its stereo correspondence in the image feature space. Chen *et al.* [54] leveraged 3D plane-swept cost volumes to reconstruct a neural encoding volume with per-voxel neural features, which is further regressed to volume density and radiance. Xu *et al.* [55] introduced scene geometry into NeRF using 3D point clouds with neural descriptors to model a radiance field.

III. PROPOSED METHOD

Overview. As shown in Fig. 2, we consider synthesizing novel views from multiple source views by reconstructing a unified 3D point cloud as the scene representation. Specifically, we first construct a sub-point cloud from each source view by projecting its pixels to 3D space based on the depth map and then fuse the sub-point clouds to build a unified one via the point cloud fusion module (Section III-A). After rendering the novel view from the unified point cloud, we restore it by filling holes and recovering high-frequency details via a 3D geometry-guided restoration module (Section III-B). In what follows, we detail each module.

A. Unified 3D Point Cloud Representation

Given N source views of dimensions $H \times W$ $\{\mathbf{I}_n \in \mathbb{R}^{W \times H}\}_{n=1}^N$ and their depth maps $\{\mathbf{D}_n \in \mathbb{R}^{W \times H}\}_{n=1}^N$, as well as the camera intrinsic and extrinsic parameters, we can project the pixels of $\{\mathbf{I}_n\}_{n=1}^N$ to a common 3D coordinate system, producing N sub-colored point clouds. Ideally, pixels of $\{\mathbf{I}_n\}_{n=1}^N$ corresponding to the same scene point should be projected to an identical 3D point. However, as $\{\mathbf{D}_n\}_{n=1}^N$ are not perfect and inevitably contain errors, such an observation cannot always be satisfied. Thus, we propose a point cloud fusion module to fuse these sub-point clouds into a unified one. As shown in Fig. 3, we first sample some anchor points from the union of sub-point clouds randomly. For each anchor point, we then seek its K nearest neighboring (KNN) points, which are further linearly interpolated with learned weights via an MLP to synthesize the point of the unified point cloud.

Specifically, let $\{\mathcal{P}_n \in \mathbb{R}^{S \times 3}\}_{n=1}^N$ denote the projected sub-point clouds corresponding to $\{\mathbf{I}_n\}_{n=1}^N$, where $S = H \times W$. We first sample M points named anchor points from the union of $\{\mathcal{P}_n \in \mathbb{R}^{S \times 3}\}_{n=1}^N$ in a random manner to construct a base point cloud $\mathcal{P}_b = \{\mathbf{x}_i \in \mathbb{R}^3\}_{i=1}^M$, i.e.,

$$\mathcal{P}_b = f_s(\mathcal{P}_1 \cup \dots \mathcal{P}_n \dots \cup \mathcal{P}_N), \quad (1)$$

where $f_s(\cdot)$ denotes the random sampling process.

For a typical anchor point $\mathbf{x}_i \in \mathcal{P}_b$, we seek its KNN from $\mathcal{P}_1 \cup \dots \mathcal{P}_N$ in the sense of Euclidean distance, denoted by $\{\mathbf{x}_i^k \in \mathbb{R}^3\}_{k=1}^K$. We then employ an MLP to learn the interpolation weight for a typical neighbor \mathbf{x}_i^k by embedding the following information.

(1) **The relative position and distance between \mathbf{x}_i^k and \mathbf{x}_i .** We define the relative position $\Delta \mathbf{x}_i^k$ and distance d_i^k as the difference and the Euclidean distance between \mathbf{x}_i^k and \mathbf{x}_i , respectively, i.e.,

$$\Delta \mathbf{x}_i^k = \mathbf{x}_i^k - \mathbf{x}_i, \text{ and } d_i^k = \|\mathbf{x}_i^k - \mathbf{x}_i\|_2, \quad (2)$$

where $\|\cdot\|_2$ denotes the ℓ_2 norm of a vector.

(2) **The descriptor similarity between \mathbf{x}_i^k and \mathbf{x}_i .** We first separately construct a descriptor for \mathbf{x}_i^k and \mathbf{x}_i , i.e.,

$$\hat{\mathbf{f}}_i^k = \text{CAT}(\mathbf{c}_i^k, \mathbf{f}_i^k), \text{ and } \hat{\mathbf{f}}_i = \text{CAT}(\mathbf{c}_i, \mathbf{f}_i), \quad (3)$$

where $\text{CAT}(\cdot)$ is the concatenation operation, and $\hat{\mathbf{f}}_i^k \in \mathbb{R}^{35}$, $\mathbf{c}_i^k \in \mathbb{R}^3$ and $\mathbf{f}_i^k \in \mathbb{R}^{32}$ (resp. $\hat{\mathbf{f}}_i \in \mathbb{R}^{35}$, $\mathbf{c}_i \in \mathbb{R}^3$ and $\mathbf{f}_i \in \mathbb{R}^{32}$) are the descriptor, the RGB values and the image feature corresponding to \mathbf{x}_i^k (resp. \mathbf{x}_i), respectively, and we learn the image features \mathbf{f}_i^k and \mathbf{f}_i from source views by employing a sub-CNN. Then, we compute the descriptor similarity s_i^k as the cosine similarity between $\hat{\mathbf{f}}_i^k$ and $\hat{\mathbf{f}}_i$, i.e.,

$$s_i^k = \frac{\hat{\mathbf{f}}_i^k \cdot \hat{\mathbf{f}}_i}{\|\hat{\mathbf{f}}_i^k\| \|\hat{\mathbf{f}}_i\|}. \quad (4)$$

We finally construct the embedding \mathbf{e}_i^k as

$$\mathbf{e}_i^k = \text{CAT}(\Delta \mathbf{x}_i^k, d_i^k, s_i^k), \quad (5)$$

and separately predict the interpolation weight $w_p^{i,k}$ and $w_f^{i,k}$ for the point position and its corresponding descriptor as

$$w_p^{i,k} = f_p(\mathbf{e}_i^k; \boldsymbol{\theta}_p), \text{ and } w_f^{i,k} = f_c(\mathbf{e}_i^k; \boldsymbol{\theta}_c), \quad (6)$$

where $f_p(\cdot; \cdot)$ and $f_c(\cdot; \cdot)$ are the learnable MLPs parameterized by $\boldsymbol{\theta}_p$ and $\boldsymbol{\theta}_c$, respectively. With the learned weights, we

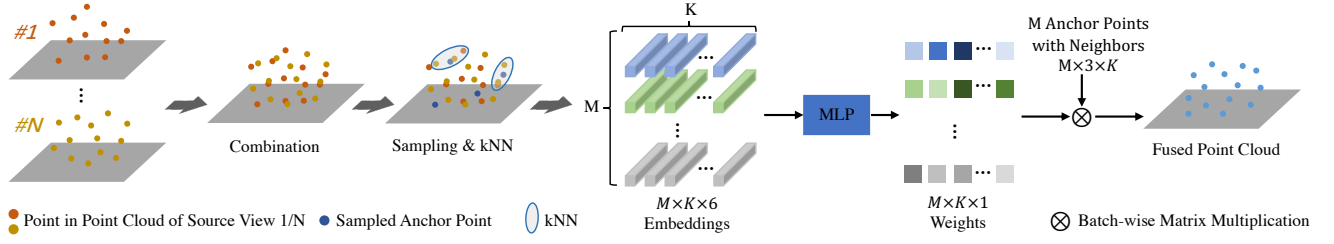


Fig. 3. Flowchart of the point cloud fusion module.

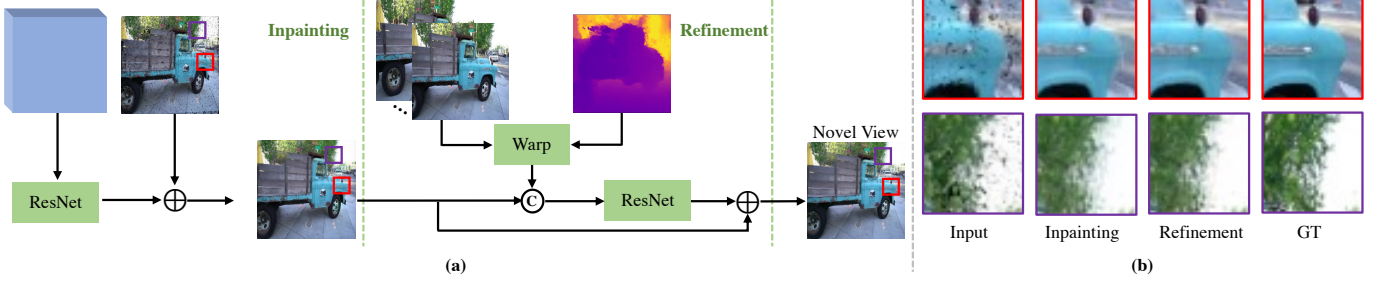


Fig. 4. (a) Flowchart of the 3D geometry-guided image restoration module. (b) Visual illustration of the effect of this module.

can obtain the point and its corresponding descriptor of the unified 3D point cloud $\tilde{\mathcal{P}} = \{\tilde{\mathbf{x}}_i \in \mathbb{R}^3\}_{i=1}^M$ as

$$\tilde{\mathbf{x}}_i = \sum_{k=1}^K w_p^{i,k} \mathbf{x}_i^k, \text{ and } \tilde{\mathbf{f}}_i = \sum_{k=1}^K w_f^{i,k} \mathbf{f}_i^k. \quad (7)$$

B. 3D Geometry-guided Image Restoration

With the unified 3D point cloud representation as well as the camera intrinsic and extrinsic parameters of the target view, we can render a coarse novel view image, denoted as $\tilde{\mathbf{I}}_t^c$, via a typical renderer. In this paper, we adopt the differentiable renderer involved in PyTorch3D [56] that splats each point to a circular region in screen-space whose opacity decreases away from the region's center and computes the value of each pixel by blending information for the neighboring points whose splatted regions overlap the pixel. However, as illustrated in the first column of Fig. 4 (b), $\tilde{\mathbf{I}}_t^c$ still suffers from holes since there are still pixel positions not in the splatted regions of any points. Besides, blending the colors of several points into one pixel also causes the missing of high-frequency details in $\tilde{\mathbf{I}}_t^c$. To deal with these issues, as shown in Fig. 4 (a), we propose a geometry-guided image restoration module to restore $\tilde{\mathbf{I}}_t^c$ by filling holes and propagating high-frequency details from the source views under the guidance of the depth map of the novel view.

Specifically, we first project $\tilde{\mathcal{P}}$ associated with descriptors to render a feature map of the novel view, denoted by $\tilde{\mathbf{F}}_t$. To fill the holes in $\tilde{\mathbf{I}}_t^c$, we learn an additive map by using a sub-CNN $f_h(\cdot; \cdot)$ parameterized by θ_h with $\tilde{\mathbf{F}}_t$ as input, i.e.,

$$\tilde{\mathbf{I}}_t^p = f_h(\tilde{\mathbf{F}}_t; \theta_h) + \tilde{\mathbf{I}}_t^c. \quad (8)$$

Furthermore, we transform $\tilde{\mathcal{P}}$ to the camera coordinate system of the novel view, and then project the points associated with

z -coordinates to render the depth map of the novel view, based on which, we separately backward warp each source view in $\{\mathbf{I}_n\}_{n=1}^N$ to the novel view, generating warped source images $\{\hat{\mathbf{I}}_n\}_{n=1}^N$. To propagate the high-frequency details from the source views to $\tilde{\mathbf{I}}_t^p$, we also learn an additive map by using another sub-CNN $f_r(\cdot; \cdot)$ parameterized by θ_r with the concatenation of $\tilde{\mathbf{I}}_t^p$ and warped source images as input, i.e.,

$$\tilde{\mathbf{I}}_t = f_r(\text{CAT}(\tilde{\mathbf{I}}_t^p, \hat{\mathbf{I}}_1, \dots, \hat{\mathbf{I}}_n, \dots, \hat{\mathbf{I}}_N); \theta_r) + \tilde{\mathbf{I}}_t^p, \quad (9)$$

where $\tilde{\mathbf{I}}_t$ is the finally synthesized novel view. As an example, Fig. 4 (b) visually illustrates the effect of the proposed 3D geometry-guided image restoration module.

C. Loss Function

We supervise both the intermediate and final rendered results by calculating the photometric loss with the ground-truth novel view \mathbf{I}_t . We define the photometric loss function $\ell_r(\cdot, \cdot)$ as

$$\ell_r(\tilde{\mathbf{I}}_t^*, \mathbf{I}_t) = \left\| \tilde{\mathbf{I}}_t^* - \mathbf{I}_t \right\|_1 + \sum_{l=1}^L \lambda_l \left\| \phi_l(\tilde{\mathbf{I}}_t^*) - \phi_l(\mathbf{I}_t) \right\|_1, \quad (10)$$

where $\|\cdot\|_1$ denotes the ℓ_1 norm, $\tilde{\mathbf{I}}_t^* \in \{\tilde{\mathbf{I}}_t^c, \tilde{\mathbf{I}}_t^p, \tilde{\mathbf{I}}_t\}$, $\{\phi_l\}_{l=1}^L$ is a set of layers in a pre-trained VGG-19 network [57], the weights $\{\lambda_l\}_{l=1}^L$ are set to the inverse of the number of neurons in each layer, and $L = 5$. Thus, the total photometric loss is calculated as

$$\hat{\ell}_r = \ell_r(\tilde{\mathbf{I}}_t^c, \mathbf{I}_t) + \ell_r(\tilde{\mathbf{I}}_t^p, \mathbf{I}_t) + \ell_r(\tilde{\mathbf{I}}_t, \mathbf{I}_t). \quad (11)$$

D. Practical Extension to the Scenario without Depth Maps

As depth maps are not always available in practice, we also extend our method by plugging a self-supervised depth estimation module, which is jointly trained with our framework. Such an extension can demonstrate the generalization ability of our method. We employ the network of MVSNet [58], a multi-view-based depth estimation network, to separately estimate the depth maps of input source views. However, MVSNet [58] requires ground-truth depth maps as supervision during training. To this end, we adopt a self-supervised loss term to regularize the learning of this network.

Specifically, to regularize MVSNet [58] generating the depth map of a typical source view, we warp other source views and the ground-truth target view to the current source view based on the estimated depth map, and then minimize the errors between the current source view and the warped images. Specifically, to estimate the depth map \mathbf{D}_n ($n \in [1, N]$) of a typical source view \mathbf{I}_n , we inversely warp other views $\{\mathbf{I}_i\}_{i=1, i \neq n}^N$ and the ground-truth novel view \mathbf{I}_t to \mathbf{I}_n based on \mathbf{D}_n , leading to the warped images $\{\mathbf{I}_{i \rightarrow n}\}_{i=1, i \neq n}^N$ and $\mathbf{I}_{t \rightarrow n}$, respectively. Formally, we write the self-supervised loss term for estimating \mathbf{D}_n as

$$\begin{aligned} \ell_{dn}^{self} = & \|(\mathbf{I}_n - \mathbf{I}_{t \rightarrow n}) \odot \mathbf{M}_{t \rightarrow n}\|_1 \\ & + \sum_{i=1}^N \|(\mathbf{I}_n - \mathbf{I}_{i \rightarrow n}) \odot \mathbf{M}_{i \rightarrow n}\|_1, i \neq n, \end{aligned} \quad (12)$$

where $\mathbf{M}_{i \rightarrow n}$ is the binary mask corresponding to $\mathbf{I}_{i \rightarrow n}$, where 0 (resp. 1) indicates the projected pixel is out of (resp. in) the range of the warped image. To further regularize the depth estimation module, apart from the $L1$ loss between the warped image and the source view, i.e., Eq. (12), we also add the SSIM loss between them. For a typical pair of warped image and source view, we define the SSIM loss function $\ell_d^{ssim}(\cdot, \cdot, \cdot)$ as

$$\ell_d^{ssim}(\mathbf{X}, \mathbf{Y}, \mathbf{M}) = \frac{1 - SSIM(\mathbf{M} \odot \mathbf{X}, \mathbf{M} \odot \mathbf{Y})}{2}, \quad (13)$$

where \mathbf{X} , \mathbf{Y} , \mathbf{M} denote the warped image, the source view, and the corresponding mask, respectively. Thus, we calculate the SSIM loss ℓ_{dk}^{ssim} for estimating \mathbf{D}_n as

$$\begin{aligned} \widehat{\ell}_{dn}^{ssim} = & \ell_d^{ssim}(\mathbf{I}_n, \mathbf{I}_{t \rightarrow n}, \mathbf{M}_{t \rightarrow n}) \\ & + \sum_{i=1}^N \ell_d^{ssim}(\mathbf{I}_n, \mathbf{I}_{i \rightarrow n}, \mathbf{M}_{i \rightarrow n}), i \neq n. \end{aligned} \quad (14)$$

Moreover, to promote smoothness of \mathbf{D}_n , we penalize the ℓ_1 norm of the gradient, denoted as ℓ_{dn}^{smooth} :

$$\ell_{dn}^{smooth} = \|\nabla_x \mathbf{D}_n\|_1 + \|\nabla_y \mathbf{D}_n\|_1, \quad (15)$$

where ∇_x and ∇_y are the gradient operators for the spatial domain. Thus, the total depth estimation loss is calculated as

$$\ell_d = \sum_{n=1}^N (\lambda_{d1} \ell_{dn}^{self} + \lambda_{d2} \widehat{\ell}_{dn}^{ssim} + \lambda_{d3} \ell_{dn}^{smooth}), \quad (16)$$

where we empirically set $\lambda_{d1} = 12$, $\lambda_{d2} = 6$, and $\lambda_{d3} = 0.18$. If we employ the self-supervised depth estimation module, we calculate the total training loss as

$$\ell = \widehat{\ell}_r + \ell_d. \quad (17)$$

Considering that estimated depth maps have deviations, we measure the depth estimation quality, namely probability map, proposed in MVSNet [58], which takes the probability sum over the four nearest depth hypotheses based on the estimated depth value to measure the estimation quality, as an added embedding term in the point cloud fusion module. We denote the depth estimation quality of \mathbf{x}_i^k by p_i^k and rewrite Eq. (5) as

$$\mathbf{e}_i^k = \text{CAT}(\Delta \mathbf{x}_i^k, d_i^k, p_i^k, s_i^k). \quad (18)$$

IV. EXPERIMENTS

A. Experiment Settings

1) *Datasets*: We conducted extensive experiments on three challenging datasets, including RealEstate10K [35], Tanks and Temples [59], and DTU [60]. All three datasets contain rotations and translations in camera movement, and particularly the first one has minor movement and the latter two are more significant.

Specifically, *RealEstate10K* is a huge dataset derived from 80k video clips and we chose a subset of 85 scenes for training and 17 scenes for testing. *Tanks and Temples* contains more complex indoor and outdoor scenes with irregular camera trajectories. Following the settings in [46], we used 17 of 21 scenes for training and the remaining four (i.e., Truck, Train, M60, and Playground) for testing. [46] also provides depth maps for *Tanks and Temples*, which were derived from a 3D surface mesh reconstructed from all views. *DTU* consists of 124 different scenes, where each was captured by 49 cameras located regularly on a sphere. We used *DTU* only for testing to verify the generalization ability. Particularly, we adopted the evaluation scene set of 18 scenes provided by Yao *et al.* [58]. [58] also provides depth maps for *DTU* by rendering the 3D mesh reconstructed from the ground-truth point cloud to each viewpoint.

2) *Implementation details*: When selecting the unstructured stereo source views for one target, we chose three consecutive frames, with the left and right frames as source views and the middle one as the target view. We implemented the encoder using Res-UNet [61] for image feature extraction and set the feature dimensions as 32. For cost volume construction in our self-supervised depth estimation module, we sampled $D = 128$ depth plane layers uniformly within the depth range of the scene. We implemented the inpainting and refinement components contained in the restoration module using ResNet with 6 blocks and 4 blocks, respectively. During training, we first trained the network without the refinement component $f_r(\cdot)$. Then, we trained the refinement component $f_r(\cdot)$ with prior network parameters fixed. We used the Adam optimizer with the learning rate equal to $1e^{-5}$.

B. Comparison with State-of-the-Art Methods

We compared our method with the three most recent view synthesis methods under the setting of synthesizing novel views from two input source views, including two image-based rendering methods, i.e., FVS [46] and SVNVS [10], and one NeRF-based method, i.e., IBRNet [50]. For fair comparisons, we retrained and evaluated these methods with

TABLE I

QUANTITATIVE COMPARISON OF DIFFERENT METHODS ON *Tanks and Temples*, *DTU* AND *RealEstate10K*. WE EXCLUDED THE FVS METHOD, POST-FUSION-D, AND OURS-D FOR *RealEstate10K* DUE TO THE LACK OF DEPTH MAPS. \uparrow (RESP. \downarrow) MEANS THE LARGER (RESP. SMALLER), THE BETTER. THE BEST RESULTS ARE HIGHLIGHTED IN BOLD.

	Tanks and Temples			DTU			RealEstate10K		
	LPIPS \downarrow	PSNR \uparrow	SSIM \uparrow	LPIPS \downarrow	PSNR \uparrow	SSIM \uparrow	LPIPS \downarrow	PSNR \uparrow	SSIM \uparrow
IBRNet [50]	0.321	19.55	0.649	0.288	19.94	0.713	0.080	29.81	0.919
SVNVs [10]	0.218	20.80	0.730	0.541	15.50	0.394	0.116	27.11	0.897
Ours-W	0.189	21.28	0.751	0.140	24.24	0.859	0.028	36.88	0.975
FVS [46]	0.302	18.91	0.661	0.236	20.14	0.723	-	-	-
Post-Fusion-D	0.155	23.47	0.848	0.193	22.50	0.823	-	-	-
Ours-D	0.139	24.44	0.856	0.162	23.70	0.844	-	-	-

TABLE II

QUANTITATIVE COMPARISON OF DIFFERENT METHODS ON THE FOUR SCENES OF *Tanks and Temples*. THE BEST RESULTS ARE HIGHLIGHTED IN BOLD.

	Train			Playground			M60			Truck		
	LPIPS \downarrow	PSNR \uparrow	SSIM \uparrow	LPIPS \downarrow	PSNR \uparrow	SSIM \uparrow	LPIPS \downarrow	PSNR \uparrow	SSIM \uparrow	LPIPS \downarrow	PSNR \uparrow	SSIM \uparrow
IBRNet [50]	0.378	17.37	0.538	0.291	23.01	0.726	0.287	18.82	0.705	0.311	19.92	0.660
SVNVs [10]	0.232	19.73	0.674	0.204	22.98	0.770	0.210	20.29	0.773	0.222	20.58	0.715
Ours-W	0.233	20.04	0.692	0.158	23.29	0.780	0.167	21.10	0.808	0.183	20.97	0.732
FVS [46]	0.341	18.22	0.597	0.286	20.91	0.696	0.354	16.28	0.633	0.180	21.32	0.768
Post-Fusion-D	0.167	21.82	0.812	0.156	26.19	0.876	0.162	22.42	0.861	0.123	24.36	0.856
Ours-D	0.161	22.41	0.821	0.128	27.35	0.883	0.134	24.16	0.886	0.124	24.61	0.858



Fig. 5. Visual comparison of different methods on *RealEstate10K*. (a) IBRNet [50], (b) SVNVs [10], (c) Ours-W, (d) Ground Truth.

the same data and settings as ours and well-tuned hyperparameters. We named our method *Ours-D* when inputting pre-processed depth maps and *Ours-W* when using self-supervised depth estimation. To directly demonstrate the effectiveness of the proposed unified 3D point cloud representation, we also constructed a baseline shown in Fig. 1(c) called *Post-Fusion-D* by replacing our point cloud fusion module with the confidence-based blending of rendered results. Specifically, we projected each source view with its features to 3D space and rendered it to the target viewpoint separately. The rendered

image was inpainted with the corresponding rendered feature map. Then we added a CNN to learn confidence maps for these inpainted images and fused them into one result further refined by warped source views. The encoding, inpainting, and refinement networks are the same as our method.

1) *Quantitative comparisons*: Table I lists the average PSNR, SSIM, and LPIPS [62] of different methods on each of the three datasets. Besides, Table II lists the results of the four scenes contained in *Tanks and Temples*. From Tables I and II, it can be observed that

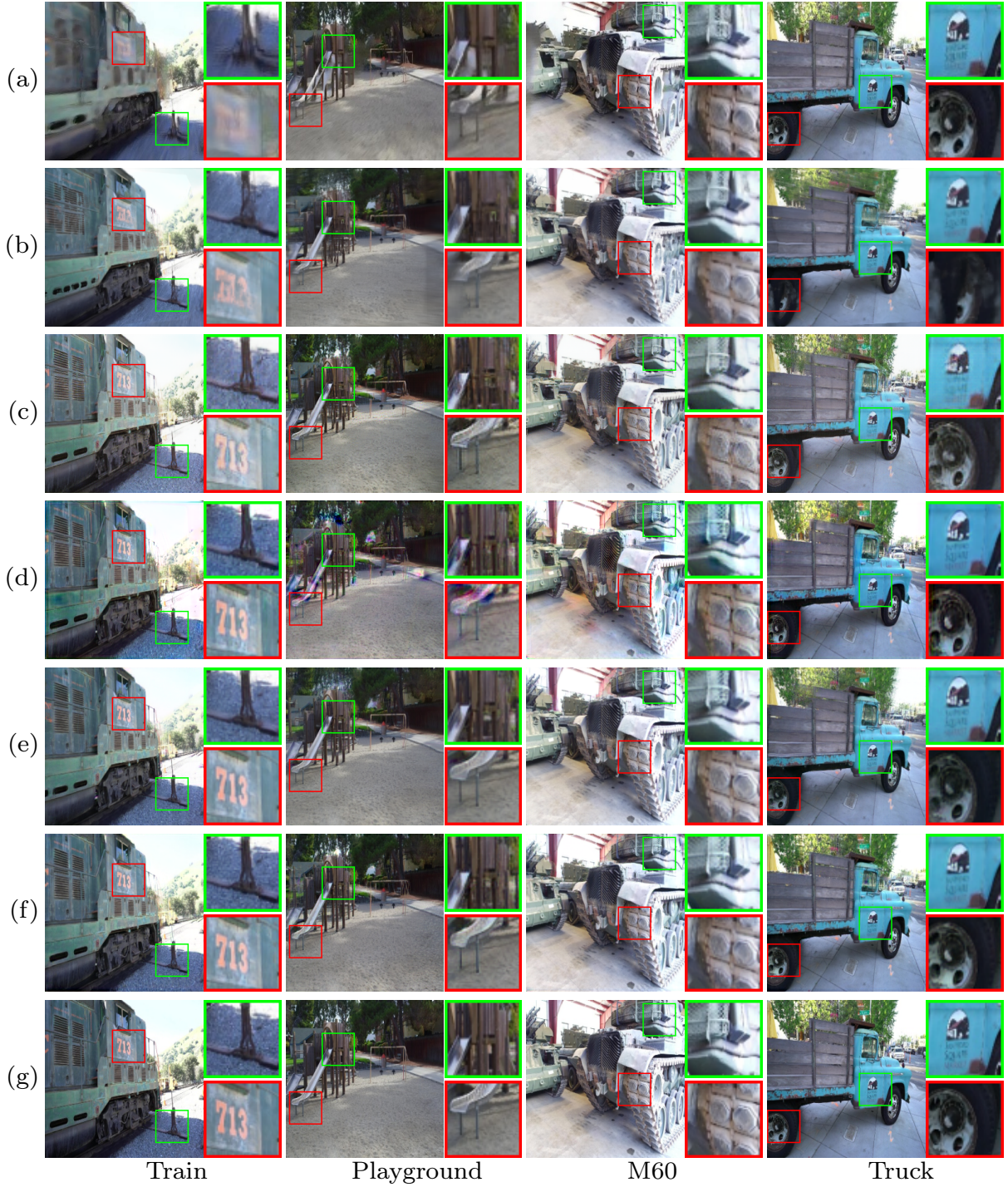


Fig. 6. Visual comparison of different methods on *Tanks and Temples*. (a) FVS [46], (b) IBRNet [50], (c) SVNVS [10], (d) Post-Fusion-D, (e) Ours-W, (f) Ours-D, (g) Ground Truth.

- both *Ours-W* and *Ours-D* consistently outperform other methods on all datasets, including both minor and significant movement, and especially *Ours-W* improves the PSNR of the second best method by more than 7 dB on *RealEstate10K*, demonstrating its significant superiority;
- we used the models trained on *Tanks and Temples* to perform testing on *DTU*. The superiority of *Ours-W* over other compared methods on *DTU* is more prominent than that on *Tanks and Temples*, demonstrating its stronger generalization ability;
- compared with the results on *Tanks and Temples*, the performance of all methods improves significantly on *RealEstate10K*. The reason may be that the camera movement of *RealEstate10K* is minor, conducive to obtaining more accurate geometry information;
- *Ours-D* improves the reconstruction quality by 1 dB compared with the baseline *Post-Fusion-D*, demonstrating the superiority of unifying sub-point clouds by our 3D point cloud fusion strategy over 2D confidence-based image blending;



Fig. 7. Visual comparison of different methods on *DTU*. (a) FVS [46], (b) IBRNet [50], (c) SVNVS [10], (d) Post-Fusion-D, (e) Ours-W, (f) Ours-D, (g) Ground Truth.

- *Ours-D* performs better than *Ours-W* on *Tanks and Temples* by more than 3dB. The reason is that self-supervised depth estimation can be challenging for datasets with large and irregular camera movements, especially when given few input images. However, *Ours-W* achieves the best performance on *DTU* because the depth maps provided in *DTU* are incomplete.

2) *Visual comparisons*: We also visually compared the results of different methods on *Tanks and Temples*, *DTU*, and *RealEstate10K* in Fig. 6, Fig. 7, and Fig. 5, respectively, where

it can be observed that our method can produce better details than all the compared methods for all datasets under the same experimental configuration. Using two source views and depth maps, the FVS can not build an accurate 3D mesh, resulting in noticeable blurred artifacts, especially on the boundaries of the synthesized image. For the IBRNet, the blurred artifacts and ghost effects appear at high-frequency regions and occlusion boundaries. As a NeRF-based method, IBRNet needs more source views to achieve satisfactory results. For SVNVS, there are blurred artifacts and slight color distortions compared with

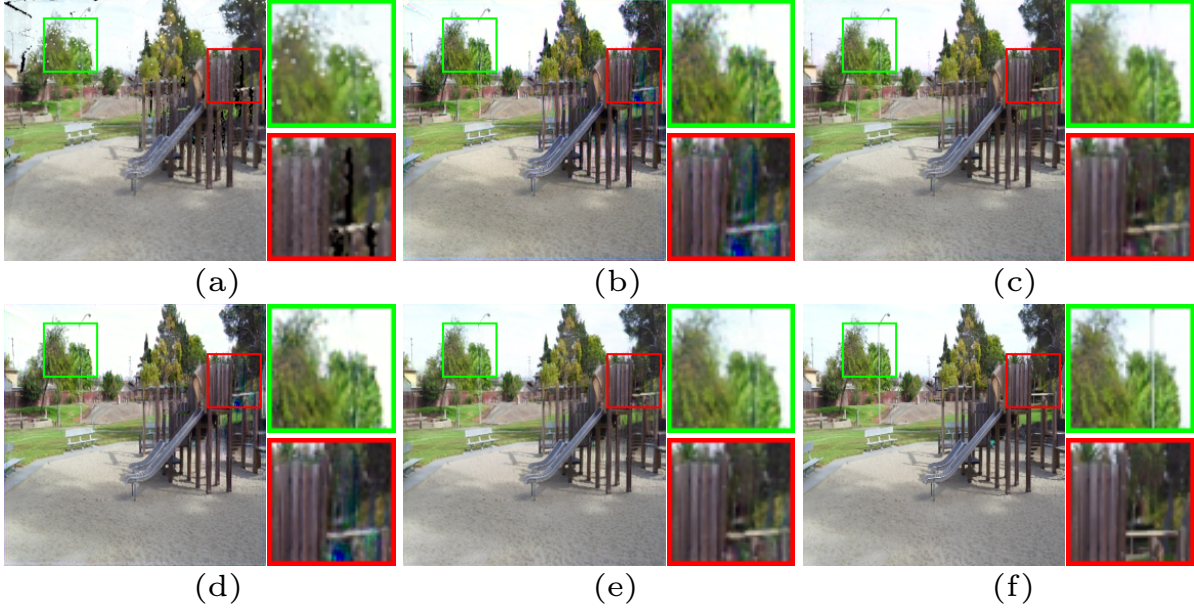


Fig. 8. Visual results of the ablation studies on network modules. (a) Baseline. (b) Baseline + Inpainting. (c) Baseline + Inpainting + Point Cloud Fusion. (d) Baseline + Inpainting + Refinement. (e) Complete model= Baseline + Inpainting + Point Cloud Fusion + Refinement. (f) Ground truth.

TABLE III
COMPARISONS OF INFERENCE TIME (IN SECONDS PER VIEW) OF
DIFFERENT METHODS ON THE DTU DATASET.

	FVS	SVNVS	IBRNet	Ours-W	Ours-D
Time (in seconds)	0.12	0.17	1.81	0.48	0.14

the ground truth. For the Post-Fusion-D, the edges of results show severe color distortions and artifacts. Additionally, Fig. 7 shows the generalization ability advantages of *Ours-W* and *Ours-D*, and both of them can get sharp and clear results.

3) *Efficiency comparisons*: Table III compares the inference time of different methods on *DTU*. Note that we implemented all methods on a Linux server with Intel CPU Xeon Gold 6226R @ 2.90GHz, 512GB RAM, and NVIDIA GeForce RTX 3090 GPU. *Ours-W* takes more time to synthesize novel views than *Ours-D* due to the self-supervised depth estimation module. *Ours-D* is slightly slower than FVS but faster than SVNVS and IBRNet. Taking the reconstruction quality and efficiency together, we believe our method is the best.

TABLE IV
QUANTITATIVE RESULTS OF THE ABLATION STUDIES. “✓” (RESP. “×”) REPRESENTS THE CORRESPONDING MODULE IS USED (RESP. UNUSED).

	Inpainting	Fusion	Refinement	LPIPS↓	PSNR↑	SSIM↑
(a)	×	×	×	0.232	19.81	0.743
(b)	✓	×	×	0.172	22.53	0.804
(c)	✓	✓	×	0.160	23.36	0.830
(d)	✓	×	✓	0.157	23.46	0.835
(e)	✓	✓	✓	0.139	24.44	0.856

C. Ablations and Analysis

1) *Network modules*: We carried out comprehensive ablation studies on *Tanks and Temples* with pre-processed depth

maps as input to validate the effectiveness of the three key components of our framework, i.e., the image inpainting component, the point cloud fusion module, and the refinement component. We constructed a baseline by excluding these three components. We sequentially added each component to the base model until all three components were included to form the complete model. When removing the point cloud fusion module, we simply merged the sub-point clouds to generate a unified point cloud to enable the method.

Quantitatively, from Table IV, it can be seen that the reconstruction quality gradually improves with the inclusion of the three components, validating their effectiveness. Qualitatively, we showed the visual results of the ablation studies in Fig. 8. Compared with the baseline result, the proposed inpainting strategy can fill the holes and fill up the unknown area in the image boundary (see Fig. 8(b)). With the proposed point cloud fusion module included, some local distortions and blurs effect are mitigated (see Fig. 8(c)). The proposed refinement module promotes the synthesized image with more high-frequency details (see Fig. 8(e)). The result of the point cloud fusion module exclusion experiment further demonstrates the effectiveness of our point fusion module (see Fig. 8(d)). We also show the results of the directly projected point clouds and the unified point clouds learned by our fusion strategy in Fig. 9, where it can be seen that the unified point cloud learned by our fusion strategy has fewer noisy points and smoother edges.

2) *Point cloud fusion embeddings*: We also validated the effectiveness of the embedded information contained in the point cloud fusion module, i.e., depth estimation quality and descriptor similarity. We conducted this experiment with our self-supervised depth module to demonstrate the effectiveness of the embedding term, depth estimation quality. As listed in Table V, it can be seen that each embedded information is

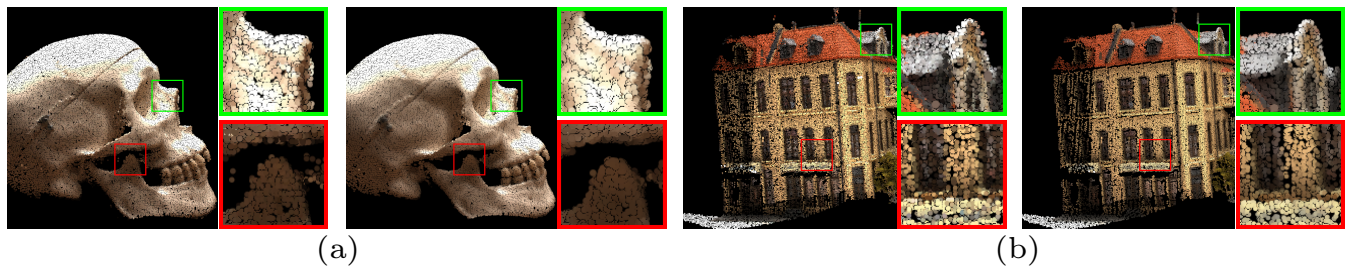


Fig. 9. Visual comparison of the 3D point clouds. The left images in (a) and (b) visualize the point clouds by directly projecting depth maps of input views into 3D space, and the right images show the point clouds learned by the proposed fusion method.

TABLE V

QUANTITATIVE RESULTS OF THE ABLATION STUDIES FOR THE EMBEDDED INFORMATION IN POINT CLOUD FUSION. “✓” (RESP. “×”) REPRESENTS THE CORRESPONDING MODULE IS USED (RESP. UNUSED).

Relative position & distance	Depth estimation quality	Descriptor similarity	LPIPS↓	PSNR↑	SSIM↑
✓	×	×	0.212	20.67	0.724
✓	✓	×	0.211	20.95	0.733
✓	✓	✓	0.189	21.28	0.751

TABLE VI

QUANTITATIVE RESULTS OF OUR METHOD WITH DIFFERENT VIEW NUMBERS ON *Tanks and Temples*.

# Input Views	Train			Playground			M60			Truck		
	LPIPS↓	PSNR↑	SSIM↑	LPIPS↓	PSNR↑	SSIM↑	LPIPS↓	PSNR↑	SSIM↑	LPIPS↓	PSNR↑	SSIM↑
2	0.161	22.41	0.821	0.128	27.35	0.883	0.134	24.16	0.886	0.124	24.61	0.858
3	0.144	23.13	0.828	0.125	27.51	0.887	0.119	24.94	0.891	0.110	25.26	0.868
4	0.145	23.23	0.831	0.128	27.49	0.887	0.115	25.02	0.893	0.107	25.23	0.870

helpful in improving the overall performance, verifying the rationality of our design.

3) *Performance of our method under various numbers of input source views*: Considering that the projected point clouds from source views are not exactly overlapping, we set $S = 1.1N$ and $K = 8$ for the 2-input setting, and $S = 1.6N$ and $K = 14$ for the 3-input setting. Due to the limited GPU memory, the proposed unified point cloud representation can’t directly process four sub-point clouds. Thus, we first fused three sub-point clouds as an intermediate unified point cloud and then fused it with the fourth point cloud. As shown in Table VI, the 3-input setting performs better than the 2-input because more information is available within the third input view. However, when given one more input view, there is no noticeable improvement. The main reason is that the camera motion in the dataset is very large, and the viewpoint of the fourth view is too far from the target view to provide useful information.

V. CONCLUSION

We have presented a new learning-based paradigm for view synthesis, which learns a unified 3D point cloud representation from multiple source views. Precisely, we constructed the unified point cloud by adaptively fusing points at a local neighborhood defined on the union of the sub-point clouds projected from source views. Owing to the learning of the unified scene representation, as well as a 3D geometry-guided image restoration module to fill the holes and recover

high-frequency details of the rendered novel view, our view synthesis paradigm reconstructs novel views with much higher quantitative and visual quality, compared with state-of-the-art methods.

REFERENCES

- [1] L. Manuelli, W. Gao, P. Florence, and R. Tedrake, “kpam: Keypoint affordances for category-level robotic manipulation,” *arXiv preprint arXiv:1903.06684*, 2019.
- [2] R. Anderson, D. Gallup, J. T. Barron, J. Kontkanen, N. Snavely, C. Hernández, S. Agarwal, and S. M. Seitz, “Jump: virtual reality video,” *ACM Transactions on Graphics (TOG)*, vol. 35, no. 6, pp. 1–13, 2016.
- [3] A. Collet, M. Chuang, P. Sweeney, D. Gillett, D. Evseev, D. Calabrese, H. Hoppe, A. Kirk, and S. Sullivan, “High-quality streamable free-viewpoint video,” *ACM Transactions on Graphics (ToG)*, vol. 34, no. 4, pp. 1–13, 2015.
- [4] S.-E. Wei, J. Saragih, T. Simon, A. W. Harley, S. Lombardi, M. Perdoch, A. Hypes, D. Wang, H. Badino, and Y. Sheikh, “Vr facial animation via multiview image translation,” *ACM Transactions on Graphics (TOG)*, vol. 38, no. 4, pp. 1–16, 2019.
- [5] T. Zhou, S. Tulsiani, W. Sun, J. Malik, and A. A. Efros, “View synthesis by appearance flow,” in *European Conference on Computer Vision (ECCV)*, 2016, pp. 286–301.
- [6] E. Park, J. Yang, E. Yumer, D. Ceylan, and A. C. Berg, “Transformation-grounded image generation network for

- novel 3d view synthesis,” in *IEEE/CVF International Conference on Computer Vision (CVPR)*, 2017, pp. 3500–3509.
- [7] S.-H. Sun, M. Huh, Y.-H. Liao, N. Zhang, and J. J. Lim, “Multi-view to novel view: Synthesizing novel views with self-learned confidence,” in *European Conference on Computer Vision (ECCV)*, 2018, pp. 155–171.
 - [8] X. Chen, J. Song, and O. Hilliges, “Monocular neural image based rendering with continuous view control,” in *IEEE/CVF International Conference on Computer Vision (CVPR)*, 2019, pp. 4090–4100.
 - [9] B. Mildenhall, P. P. Srinivasan, M. Tancik, J. T. Barron, R. Ramamoorthi, and R. Ng, “Nerf: Representing scenes as neural radiance fields for view synthesis,” in *European conference on computer vision (ECCV)*, 2020, pp. 405–421.
 - [10] Y. Shi, H. Li, and X. Yu, “Self-supervised visibility learning for novel view synthesis,” in *IEEE/CVF Conference on Computer Vision and Pattern Recognition (CVPR)*, 2021, pp. 9675–9684.
 - [11] M. Meshry, D. B. Goldman, S. Khamis, H. Hoppe, R. Pandey, N. Snively, and R. Martin-Brualla, “Neural rerendering in the wild,” in *IEEE/CVF Conference on Computer Vision and Pattern Recognition (CVPR)*, 2019, pp. 6878–6887.
 - [12] F. Pittaluga, S. J. Koppal, S. B. Kang, and S. N. Sinha, “Revealing scenes by inverting structure from motion reconstructions,” in *IEEE/CVF Conference on Computer Vision and Pattern Recognition (CVPR)*, 2019, pp. 145–154.
 - [13] K.-A. Aliev, A. Sevastopolsky, M. Kolos, D. Ulyanov, and V. Lempitsky, “Neural point-based graphics,” in *European Conference on Computer Vision (ECCV)*, 2020, pp. 696–712.
 - [14] P. Dai, Y. Zhang, Z. Li, S. Liu, and B. Zeng, “Neural point cloud rendering via multi-plane projection,” in *IEEE/CVF Conference on Computer Vision and Pattern Recognition (CVPR)*, 2020, pp. 7830–7839.
 - [15] Z. Song, W. Chen, D. Campbell, and H. Li, “Deep novel view synthesis from colored 3d point clouds,” in *European Conference on Computer Vision (ECCV)*, 2020, pp. 1–17.
 - [16] D. Rückert, L. Franke, and M. Stamminger, “Adop: Approximate differentiable one-pixel point rendering,” *ACM Transactions on Graphics (TOG)*, 2022.
 - [17] S. Niklaus, L. Mai, J. Yang, and F. Liu, “3d ken burns effect from a single image,” *ACM Transactions on Graphics (TOG)*, vol. 38, no. 6, pp. 1–15, 2019.
 - [18] O. Wiles, G. Gkioxari, R. Szeliski, and J. Johnson, “Synsin: End-to-end view synthesis from a single image,” in *IEEE/CVF Conference on Computer Vision and Pattern Recognition (CVPR)*, 2020, pp. 7467–7477.
 - [19] H. Le, T. Mensink, P. Das, and T. Gevers, “Novel view synthesis from single images via point cloud transformation,” in *Proceedings of the British Machine Vision Conference (BMVC)*, 2020.
 - [20] A. Cao, C. Rockwell, and J. Johnson, “Fwd: Real-time novel view synthesis with forward warping and depth,” in *Proceedings of the IEEE/CVF Conference on Computer Vision and Pattern Recognition*, 2022, pp. 15 713–15 724.
 - [21] C. Buehler, M. Bosse, L. McMillan, S. Gortler, and M. Cohen, “Unstructured lumigraph rendering,” in *Proceedings of the 28th annual conference on Computer graphics and interactive techniques*, 2001, pp. 425–432.
 - [22] P. E. Debevec, C. J. Taylor, and J. Malik, “Modeling and rendering architecture from photographs: A hybrid geometry-and image-based approach,” in *Proceedings of the 23rd annual conference on Computer graphics and interactive techniques*, 1996, pp. 11–20.
 - [23] S. J. Gortler, R. Grzeszczuk, R. Szeliski, and M. F. Cohen, “The lumigraph,” in *Proceedings of the 23rd annual conference on Computer graphics and interactive techniques*, 1996, pp. 43–54.
 - [24] M. Levoy and P. Hanrahan, “Light field rendering,” in *Proceedings of the 23rd annual conference on Computer graphics and interactive techniques*, 1996, pp. 31–42.
 - [25] S. M. Seitz and C. R. Dyer, “View morphing,” in *Proceedings of the 23rd annual conference on Computer graphics and interactive techniques*, 1996, pp. 21–30.
 - [26] X. Yan, J. Yang, E. Yumer, Y. Guo, and H. Lee, “Perspective transformer nets: Learning single-view 3d object reconstruction without 3d supervision,” *Advances in Neural Information Processing Systems*, vol. 29, pp. 1696–1704, 2016.
 - [27] C. B. Choy, D. Xu, J. Gwak, K. Chen, and S. Savarese, “3d-r2n2: A unified approach for single and multi-view 3d object reconstruction,” in *European conference on computer vision*, 2016, pp. 628–644.
 - [28] D. Jimenez Rezende, S. Eslami, S. Mohamed, P. Battaglia, M. Jaderberg, and N. Heess, “Unsupervised learning of 3d structure from images,” *Advances in neural information processing systems*, vol. 29, pp. 4996–5004, 2016.
 - [29] A. Kar, C. Häne, and J. Malik, “Learning a multi-view stereo machine,” in *International Conference on Neural Information Processing Systems (NIPS)*, 2017, pp. 364–375.
 - [30] E. Penner and L. Zhang, “Soft 3d reconstruction for view synthesis,” *ACM Transactions on Graphics (TOG)*, vol. 36, no. 6, pp. 1–11, 2017.
 - [31] H. Xie, H. Yao, X. Sun, S. Zhou, and S. Zhang, “Pix2vox: Context-aware 3d reconstruction from single and multi-view images,” in *IEEE/CVF International Conference on Computer Vision (CVPR)*, 2019, pp. 2690–2698.
 - [32] P. Henzler, N. J. Mitra, and T. Ritschel, “Escaping plato’s cave: 3d shape from adversarial rendering,” in *IEEE/CVF International Conference on Computer Vision (CVPR)*, 2019, pp. 9984–9993.
 - [33] S. Lombardi, T. Simon, J. Saragih, G. Schwartz, A. Lehrmann, and Y. Sheikh, “Neural volumes: learning dynamic renderable volumes from images,” *ACM Transactions on Graphics (TOG)*, vol. 38, no. 4, pp. 1–14, 2019.
 - [34] V. Sitzmann, J. Thies, F. Heide, M. Nießner, G. Wetzstein, and M. Zollhofer, “Deepvoxels: Learning persistent 3d feature embeddings,” in *IEEE/CVF Conference*

- on *Computer Vision and Pattern Recognition (CVPR)*, 2019, pp. 2437–2446.
- [35] T. Zhou, R. Tucker, J. Flynn, G. Fyffe, and N. Snavely, “Stereo magnification: learning view synthesis using multiplane images,” *ACM Transactions on Graphics (TOG)*, vol. 37, no. 4, pp. 1–12, 2018.
 - [36] J. Flynn, M. Broxton, P. Debevec, M. DuVall, G. Fyffe, R. Overbeck, N. Snavely, and R. Tucker, “Deep-view: View synthesis with learned gradient descent,” in *IEEE/CVF Conference on Computer Vision and Pattern Recognition (CVPR)*, 2019, pp. 2367–2376.
 - [37] B. Mildenhall, P. P. Srinivasan, R. Ortiz-Cayon, N. K. Kalantari, R. Ramamoorthi, R. Ng, and A. Kar, “Local light field fusion: Practical view synthesis with prescriptive sampling guidelines,” *ACM Transactions on Graphics (TOG)*, vol. 38, no. 4, pp. 1–14, 2019.
 - [38] P. P. Srinivasan, R. Tucker, J. T. Barron, R. Ramamoorthi, R. Ng, and N. Snavely, “Pushing the boundaries of view extrapolation with multiplane images,” in *IEEE/CVF Conference on Computer Vision and Pattern Recognition (CVPR)*, 2019, pp. 175–184.
 - [39] Z. Li, W. Xian, A. Davis, and N. Snavely, “Crowdsampling the plenoptic function,” in *European Conference on Computer Vision (ECCV)*, 2020, pp. 178–196.
 - [40] J. Shade, S. Gortler, L.-w. He, and R. Szeliski, “Layered depth images,” in *Proceedings of the 25th annual conference on Computer graphics and interactive techniques*, 1998, pp. 231–242.
 - [41] L. Świrski, C. Richardt, and N. A. Dodgson, “Layered photo pop-up,” in *ACM SIGGRAPH 2011 Posters*, 2011, pp. 1–1.
 - [42] S. Tulsiani, R. Tucker, and N. Snavely, “Layer-structured 3d scene inference via view synthesis,” in *Proceedings of the European Conference on Computer Vision (ECCV)*, 2018, pp. 302–317.
 - [43] M.-L. Shih, S.-Y. Su, J. Kopf, and J.-B. Huang, “3d photography using context-aware layered depth inpainting,” in *IEEE/CVF Conference on Computer Vision and Pattern Recognition (CVPR)*, 2020, pp. 8028–8038.
 - [44] H. Dhano, N. Navab, and F. Tombari, “Object-driven multi-layer scene decomposition from a single image,” in *IEEE/CVF International Conference on Computer Vision (CVPR)*, 2019, pp. 5369–5378.
 - [45] I. Choi, O. Gallo, A. Troccoli, M. H. Kim, and J. Kautz, “Extreme view synthesis,” in *IEEE/CVF International Conference on Computer Vision (CVPR)*, 2019, pp. 7781–7790.
 - [46] G. Riegler and V. Koltun, “Free view synthesis,” in *European Conference on Computer Vision (ECCV)*, 2020, pp. 623–640.
 - [47] G. Riegler and V. Koltun, “Stable view synthesis,” in *IEEE/CVF Conference on Computer Vision and Pattern Recognition (CVPR)*, 2021, pp. 12 216–12 225.
 - [48] R. Martin-Brualla, N. Radwan, M. S. Sajjadi, J. T. Barron, A. Dosovitskiy, and D. Duckworth, “Nerf in the wild: Neural radiance fields for unconstrained photo collections,” in *IEEE/CVF Conference on Computer Vision and Pattern Recognition (CVPR)*, 2021, pp. 7210–7219.
 - [49] A. Yu, V. Ye, M. Tancik, and A. Kanazawa, “pixelnerf: Neural radiance fields from one or few images,” in *IEEE/CVF Conference on Computer Vision and Pattern Recognition (CVPR)*, 2021, pp. 4578–4587.
 - [50] Q. Wang, Z. Wang, K. Genova, P. P. Srinivasan, H. Zhou, J. T. Barron, R. Martin-Brualla, N. Snavely, and T. Funkhouser, “Ibrnet: Learning multi-view image-based rendering,” in *IEEE/CVF Conference on Computer Vision and Pattern Recognition (CVPR)*, 2021, pp. 4690–4699.
 - [51] A. Trevithick and B. Yang, “Grf: Learning a general radiance field for 3d representation and rendering,” in *IEEE/CVF International Conference on Computer Vision (CVPR)*, 2021, pp. 15 182–15 192.
 - [52] J. Chibane, A. Bansal, V. Lazova, and G. Pons-Moll, “Stereo radiance fields (srf): Learning view synthesis from sparse views of novel scenes,” in *IEEE/CVF International Conference on Computer Vision (CVPR)*, 2021, pp. 7907–7916.
 - [53] J. Li, Z. Feng, Q. She, H. Ding, C. Wang, and G. H. Lee, “Mine: Towards continuous depth mpi with nerf for novel view synthesis,” in *IEEE/CVF International Conference on Computer Vision (CVPR)*, 2021, pp. 12 578–12 588.
 - [54] A. Chen, Z. Xu, F. Zhao, X. Zhang, F. Xiang, J. Yu, and H. Su, “Mvsnerf: Fast generalizable radiance field reconstruction from multi-view stereo,” in *Proceedings of the IEEE/CVF International Conference on Computer Vision*, 2021, pp. 14 124–14 133.
 - [55] Q. Xu, Z. Xu, J. Philip, S. Bi, Z. Shu, K. Sunkavalli, and U. Neumann, “Point-nerf: Point-based neural radiance fields,” in *Proceedings of the IEEE/CVF Conference on Computer Vision and Pattern Recognition*, 2022, pp. 5438–5448.
 - [56] N. Ravi, J. Reizenstein, D. Novotný, T. Gordon, W.-Y. Lo, J. Johnson, and G. Gkioxari, “Accelerating 3d deep learning with pytorch3d,” *SIGGRAPH Asia 2020 Courses*, 2020.
 - [57] K. Simonyan and A. Zisserman, “Very deep convolutional networks for large-scale image recognition,” *International Conference on Learning Representations*, 2014.
 - [58] Y. Yao, Z. Luo, S. Li, T. Fang, and L. Quan, “Mvsnet: Depth inference for unstructured multi-view stereo,” in *European Conference on Computer Vision (ECCV)*, 2018, pp. 767–783.
 - [59] A. Knapitsch, J. Park, Q.-Y. Zhou, and V. Koltun, “Tanks and temples: Benchmarking large-scale scene reconstruction,” *ACM Transactions on Graphics (ToG)*, vol. 36, no. 4, pp. 1–13, 2017.
 - [60] H. Aanæs, R. R. Jensen, G. Vogiatzis, E. Tola, and A. B. Dahl, “Large-scale data for multiple-view stereopsis,” *International Journal of Computer Vision (IJCV)*, vol. 120, no. 2, pp. 153–168, 2016.
 - [61] X. Xiao, S. Lian, Z. Luo, and S. Li, “Weighted res-unet for high-quality retina vessel segmentation,” in *International conference on information technology in medicine and education (ITME)*, 2018, pp. 327–331.
 - [62] R. Zhang, P. Isola, A. A. Efros, E. Shechtman, and O. Wang, “The unreasonable effectiveness of deep fea-

tures as a perceptual metric,” in *IEEE/CVF International Conference on Computer Vision (CVPR)*, 2018, pp. 586–595.